Engineered Science
DOI: https://dx.doi.org/10.30919/es1671

Corrosion Inhibition of Eco-Friendly Agricultural Waste-based *Prinsepia utilis Royle* Meal Extract for Cold-Rolled Steel in Acidic Media: Experimental and Simulation

Liqing Tang,[1,3] Min Tang,[1,3] Ping Zhu,[3,4] Xianghong Li,[1,3,*] Yun Gao,[1,3] Yi Zhang,[1,3] Yingju Miao[2,*] and Juan Xu[1,3,*]

Abstract

Utilizing agricultural and forestry waste as plant-derived corrosion inhibitors can alleviate resource scarcity and environmental pollution. In this study, *Prinsepia utilis Royle meal* extract (PURME) was extracted via 60% ethanol reflux, and its corrosion inhibition on cold-rolled steel (CRS) in 0.5 M H_2SO_4 and 1.0 M HCl was evaluated through weight loss, electrochemical tests, FTIR (Fourier Transform Infrared Spectroscopy), LC-MS (Liquid Chromatography-Mass Spectrometry), UV-vis (Ultraviolet-Visible Spectroscopy), and conductivity measurements. Surface analysis employed XPS (X-ray Photoelectron Spectroscopy), AFM (Atomic Force Microscopy), contact angle, and TOF-SIMS (Time-of-Flight Secondary Ion Mass Spectrometry). The results demonstrated that PURME achieved inhibition efficiencies of 89.25% in H_2SO_4 and 91.28% in HCl at 20°C, conforming to the Langmuir adsorption model. Electrochemical tests revealed PURME as a mixed-type inhibitor with predominant cathodic inhibition. LC-MS identified key active components, such as chenodeoxycholic acid and linolenic acid, while FTIR, XPS, and TOF-SIMS confirmed the adsorption of functional groups (-C-N, -C-O, -OH) onto CRS surfaces. AFM and contact angle measurements further validated PURME's corrosion inhibition efficacy. Computational analyses (QC (quantum chemical) calculations and MD (molecular dynamics) simulations) revealed that reactive sites were primarily localized on -COOH, -OH, and C=C groups, elucidating the adsorption mechanism. These findings systematically highlight PURME's potential as an eco-friendly corrosion inhibitor in acidic environments.

Keywords: Prinsepia utilis Royle; Agricultural waste; Corrosion inhibitor; Adsorption.
Received: 26 May 2025; Revised: 21 July 2025; Accepted: 22 July 2025
Article type: Research article.

1. Introduction

One of the most widely used and abundant metals in the world is steel.[1] According to reliable estimates, global steel demand will reach approximately 1.8 billion tons by 2025.[2] Immersion treatment of uncorroded steel in passivation solution is a common means of corrosion prevention.[3] As for the corroded steel, if not addressed in time, the corrosion will further corrode the substrate and cause more serious damage. Pickling is the key method of rust removal.[4] H_2SO_4 and HCl, which are stable and affordable, are still the most widely used pickling solutions in industry.[5,6] However, due to the inherent corrosiveness of acids, the cleaning process often results in the undesirable "over-etching" of the metal substrate while removing surface rust. Adding corrosion inhibitors can effectively mitigate this issue, preventing the metal material from being excessively corroded during the pickling process.[7]

Traditional inorganic inhibitors demonstrate remarkable effectiveness in protecting various metallic materials. However, these substances typically contain heavy metals, rendering them highly toxic and poorly biodegradable. For example, chromate-based inhibitors exhibit outstanding corrosion inhibition performance and broad applicability. However, their high water solubility and strong mobility result in persistent environmental retention after discharge, posing severe threats to ecosystems, human health, and animal welfare. Notably, hexavalent chromium (Cr^{6+}), classified as a Group 1 carcinogen by the International Agency for Research on Cancer (IARC), may induce lung cancer, sinus cancer, and other malignancies upon chronic exposure.[8] As societal awareness of environmental protection grows, regulatory

[1]*College of Materials and Chemical Engineering, Southwest Forestry University, Kunming, 650224, China*
[2]*School of Chemistry and Materials Engineering, Liupanshui Normal University, Liupanshui, Guizhou, 553004, China*
[3]*National Joint Engineering Research Center for Highly-Efficient Utilization Technology of Forestry Resources; Southwest Forestry University, Kunming, 650224, China*

agencies have imposed strict limits on the use and emissions of such inhibitors, significantly restricting their applications. Plant-extracted inhibitors demonstrate unique advantages over synthetic counterparts in organic corrosion inhibitor systems. Their extraction processes typically follow green chemistry principles, utilizing mild physical methods such as room-temperature maceration, solvothermal reflux, and ultrasound-assisted extraction for efficient active component enrichment. This preparation strategy avoids the harsh reaction conditions and high energy consumption of complex organic synthesis while significantly reducing material and equipment costs. [9,10] From a sustainability perspective, plant extracts exhibit exceptional diversity and renewability. Various plant biomass organs-including stems, leaves, fruits, and peels-can serve as extraction sources.

Many of them have been recognized as effective, including *Mikania micranth*,[11] *Eupatorium Adenophora* (Spreng.) leaves,[12] *White turnip* bark,[13] *spinach,*[14] *maple* leaves,[15] *reed* leaves,[16] *Sunflower* head pectin,[17] *blackberry* leaves,[18] *Rheum ribes* leaves,[19] *Combined* clove,[20] *Dendrocalamus brandisii* leaves,[21] *Locust Bean Gum,*[22] etc. among others. This "whole-plant utilization" approach significantly expands the range of potential raw materials while providing a viable pathway for the value-added utilization of agricultural byproducts. Amino acids, tannins, phenolics, glycosides and others in extracts play a critical role in corrosion inhibition.[23] These phytochemicals exhibit strong adsorption onto metal surfaces via electron-rich sites, heterocyclic structures. Their polar functional groups contribute significantly to stable adsorption on metal surfaces, providing effective and sustainable corrosion protection.[24] Current research primarily focuses on employing agricultural and forestry waste as feedstock for plant-based corrosion inhibitors. This strategy not only adds economic value to waste materials but also mitigates environmental pollution associated with waste disposal.

Prinsepia utilis Royle is a perennial shrub of the Rosaceae family that has been used in China for thousands of years. It is mainly found at high altitudes.[25] It is a valuable oil plant and *Printespia utilis Royle* oil is widely used in medicine, food, skin care and health care products. A by-product of the *Prinsepia utilis Royle* oil extraction process is meal, but so far it has not been effectively utilized.[26] With 0.8 kg of the oil meal obtained for every 1 kg of *Prinsepia utilis Royle* that is pressed for oil.[27] However, for a long time, this by-product was either returned to the soil as fertilizer or discarded, resulting in a serious waste of valuable resources. It contains a large number of fatty acids and other substances containing unsaturated polar groups, and it can be assumed that it has a good corrosion inhibition effect.[28]

To systematically manage this abundant oil meal resource, we propose for the first time the use of PURME as a novel corrosion inhibitor in acidic media (H_2SO_4 and HCl), investigating its protective effects on cold-rolled steel. The active constituents of PURME were characterized by LC-MS and FTIR techniques. Preliminary evaluation of its corrosion inhibition performance was conducted through weight loss measurements and electrochemical analyses, with further validation via advanced characterization methods including AFM, XPS, TOF-SIMS and contact angle measurements. By subjecting the active ingredients to QC calculations and MD simulations, and synergistically combining experimental characterization with theoretical calculations, we have systematically elucidated the mechanistic basis of the corrosion inhibition behavior of PURME.

2. Experimental process

2.1 Materials and solutions

CRS (0.8 mm thickness, Panzhihua Steel Plant) samples were sequentially polished using 60 to 2000-mesh abrasive paper and sectioned into 25 mm × 20 mm specimens prior to testing.

2.2 Preparation and compositional analysis of PURME

The preparation procedure is shown in Fig. 1. After drying and crushing PURM, ultrasonic assisted extraction was performed twice with 60% ethanol solution at 50 °C for 30 min each time. The filtrate was filtered and combined, then concentrated and lyophilized to obtain PURME, which is brownish green in color and viscous, easily soluble in water. The extraction yield of PURME was 20.2 %.

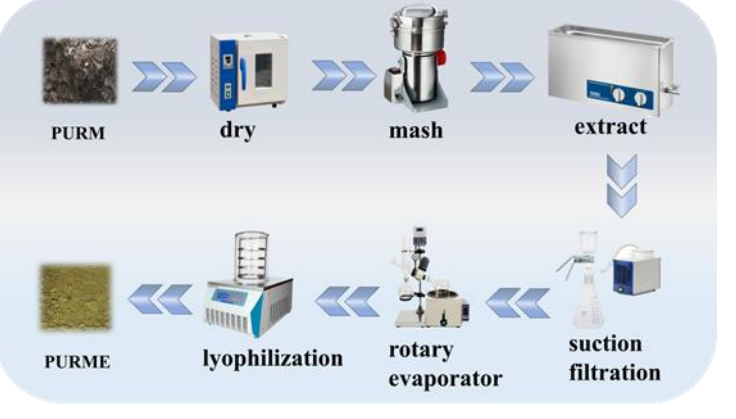

Fig. 1: PURME extraction flowchart.

LC-MS (WatersADC, USA) was used to analyzed the main components of PURME. FTIR (AVATAR-FTIR-360, USA) was employed to identify the functional groups. For FTIR analysis, the samples were homogenously mixed with KBr powder at a ratio of 1:100.

2.3 Analysis of solution properties

The conductivity and UV-vis absorption curves were tested by conductivity meter (PE38, Shanghai) and ultraviolet-visible

[4]*Yunnan Provincial Special Equipment Safety Testing and Research Institute, Kunming, 650228, China*
**E-mail:* xianghong-li@163.com (Xianghong Li),
egomyj@163.com (Yingju Miao),
58045846@qq.com (Juan Xu)

spectrometer (UNICO UV-2800A, Shanghai). The reference solution was prepared using distilled water as the solvent, and UV-Vis spectral measurements were performed across the wavelength range of 190-400 nm.

2.4 Surface test of CRS

XPS (K-Alpha+) and AFM (Bruker Dimension Icon, Germany), contact angle (Dataphysics OCA20, Germany), and TOF-SIMS (PHI nano TOFII, Japan) were used for surface analysis.

2.5 Weight loss method

At a certain temperature, the precisely weighed CRS was immersed in 0.5 M H_2SO_4 or 1 M HCl media containing various concentrations of PURME. After 6 hours, the CRS was taken out, the surface corrosion products were removed, the specimen was dried and weighed. The results were replicated three times to minimize experimental errors.

2.6 Electrochemical test

Electrochemical tests were carried out at 20 ℃ (CHI760E, Shanghai). First, the open-circuit potentials (OCP) were measured for 30 min to ensure potential stability. Electrochemical impedance spectroscopy (EIS) was measured in the frequency range from 10^{-2} to 10^5 Hz. Tafel polarization measurements were carried out within a potential window of ±250 mV relative to the OCP.

2.7 Theoretical calculation

A systematic molecular optimization of chenodeoxycholic acid, linolenic acid, and their respective protonated forms was carried out using the DMol3 module of Materials Studio 7.0 software. Subsequently, the frontier molecular orbitals and Fukui functions were calculated, and the local reaction sites of these molecules were analyzed. MD simulations were performed in the Discover module of the software. The adsorption of the aforementioned molecules on the Fe(110) surface was studied with water as the solvent at a reaction temperature of 298 K. The entire simulation was conducted under the COMPASS II force field and NVT ensemble, with a time step of 1.0 fs and a total simulation time of 1000 ps.[29,30]

3. Results and discussion

3.1 Component analysis

Plants contain many chemical components, and clarification of their active ingredients facilitates in-depth discussion of corrosion inhibition properties and mechanisms.

Fig. 2(a) presents the positive and negative ion scans obtained from the LC-MS analysis of PURME. Comparative database analysis identified the presence of significant quantities of sanleng acid, chenodeoxycholic acid, procyanidin B3, ganoderic acid H, linolenic acid, citric acid, dibutyl sebacate, and malvalic acid in the extract and the molecular structures are illustrated in Fig. 2(b).

Fig. 2(c) displays the FTIR spectra of PURME. The prominent absorption band observed at 3356 cm^{-1} is attributed to the stretching vibrations of N-H/O-H groups. The sharp absorption band at 2927 cm^{-1} arises from the C-H stretching vibrations. Additionally, the absorption band at 1605 cm^{-1} is likely associated with the stretching vibrations of C=O or C=C functional groups.[31] The stretching vibration at 1405 cm^{-1} is caused by $-CH_3$. There is a distinct absorption band at 1035 cm^{-1} which can be attributed to the stretching vibration of the -C-O- bond.[20] The absorption bands observed below 1000 cm^{-1} are attributed to the substitution fingerprint regions of benzene or heteroaromatic rings. These functional groups suggest that the compounds in PURME contain polar groups with a significant number of lone pair electrons.

3.2 Properties of corrosion inhibition solution and UV analysis

The conductivity was measured under different experimental conditions. Conductivity reflects a solution's ability to transfer electric current, where a higher degree of ion dissociation corresponds to increased conductivity and improved charge transfer properties. Fig. 2(d) shows the conductivity values of the corrosion inhibitor solution under various conditions, following the trend of κ (PURME+HCl)> κ (PURME+HCl+CRS) > κ (PURME+H_2SO_4) > κ (PURME+H_2SO_4+CRS) > κ (PURME). The plant-derived PURME extract is inherently difficult to ionize, exhibiting near-zero conductivity. However, PURME can combine with H^+ ions in solution to form positively charged $PURMEH_x^{x+}$ cations, which subsequently associate with anions such as SO_4^{2-}/Cl^-. Weight loss measurements demonstrate that hydrochloric acid exhibits weaker corrosivity toward cold-rolled steel (CRS) than sulfuric acid, while PURME shows comparable inhibition efficiency in both acidic media. This observation indicates preferential interaction between $PURMEH_x^{x+}$ and SO_4^{2-}, which satisfactorily explains why κ (PURME+HCl)>κ (PURME+H_2SO_4). Post-corrosion, the generated $FeSO_4$ and $FeCl_2$ adsorb onto the CRS surface, reducing their concentrations in the liquid phase. At the same time, the adsorption of PURME on the metal surface further suppresses corrosion reactions. Consequently, the solution conductivity shows a slight decrease after reaction and remains virtually unchanged with increasing PURME concentration.

Fig. 2(e) presents the UV-Vis spectral curves under different conditions. Without PURME addition, comparison of the spectra before and after the CRS corrosion reveals a significant red shift in the maximum absorption peak along with increased absorbance. Upon PURME addition, distinct absorption peaks emerge at 318 nm (in H_2SO_4) and 310 nm (in HCl), corresponding to the n-π* transition of C=N bonds. The red shift phenomenon becomes markedly enhanced following PURME addition and subsequent reaction with CRS. This pronounced spectral shift, accompanied by elevated absorbance, is principally attributed to intermolecular interactions and steric hindrance effects arising from molecu-

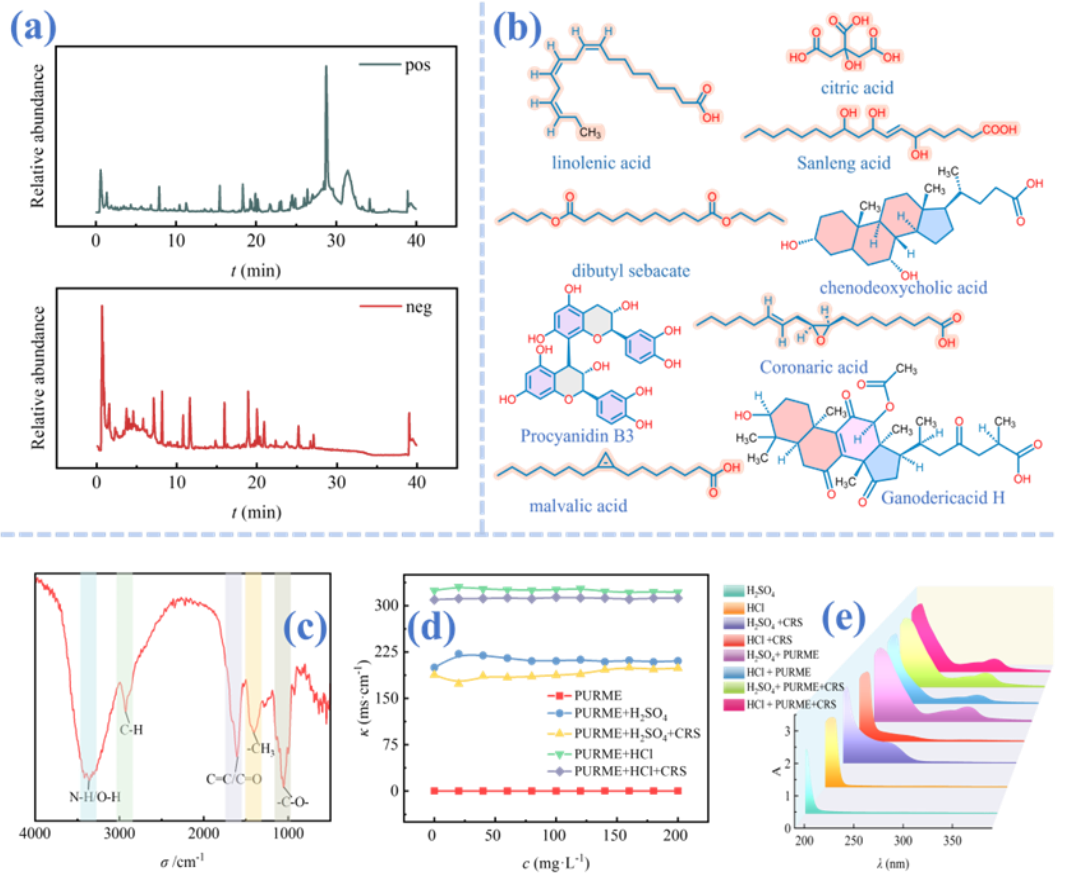

Fig. 2: Total ion current diagram of PURME by LC-MS (a) and the main chemical compounds in PURME (b), FTIR spectra of PURME(c), the relationships between electrical conductivity with PURME concentration at 20 ℃ (d) and UV-vis absorption curves (e).

lar-level structural modifications. These experimental observations demonstrate that specific PURME-CRS interactions significantly influence optical properties, reflecting substantial alterations in both electronic environment and molecular configuration.

3.3 Weight loss method

The corresponding corrosion rate (v) and inhibition efficiency (η_W) were calculated according to Eq. (1) and (2),[31] respectively.

$$v = \frac{W}{S \times t} \quad (1)$$

where W is the difference in quality of CRS before and after reaction (g), S is the reaction area (m^2), and t is the immersion time (h).

$$\eta_w = \frac{v_0 - v}{v_0} \times 100\% \quad (2)$$

where v_0 and v are corrosion rates ($g \cdot m^{-2} \cdot h^{-1}$) in both acidic environments without and with PURME.

As shown in Fig. 3(a) and 3(b), the corrosion rate and inhibition efficiency were measured in 0.5 M H_2SO_4 and 1.0 M HCl solutions containing different concentrations of PURME. The corrosion rate in both acidic media increases significantly with temperature elevation from 20 to 50°C, reaching maximum values of 76.61 and 52.99 $g \cdot m^{-2} \cdot h^{-1}$, respectively. This temperature-dependent acceleration of corrosion can be attributed to enhanced molecular thermal motion, which promotes metal dissolution. With PURME addition, the corrosion rate decreases progressively, showing a concentration-dependent inhibition effect. The maximum inhibition efficiencies of 89.25% (H_2SO_4) and 91.28% (HCl) were achieved at 20°C with 200 $mg \cdot L^{-1}$ PURME concentration.

3.4 Adsorption isotherm

The Langmuir,[33] Freundlich[32] and Temkin[34] adsorption isotherms were employed to fit the adsorption behavior of PURME on the surface of CRS in two solutions, and the empirical equations are shown in Eq. (3-5), respectively. The relevant values obtained are listed in Table 1.

The Langmuir adsorption models are presented in Fig. 4(a1) and 4(b1), respectively. In the H_2SO_4 medium, both the slopes of the linear correlation coefficients and the fitted regression lines approach unity more closely at lower temperatures, indicating enhanced PURME adsorption under these conditions. With increasing temperature, the intermolecular

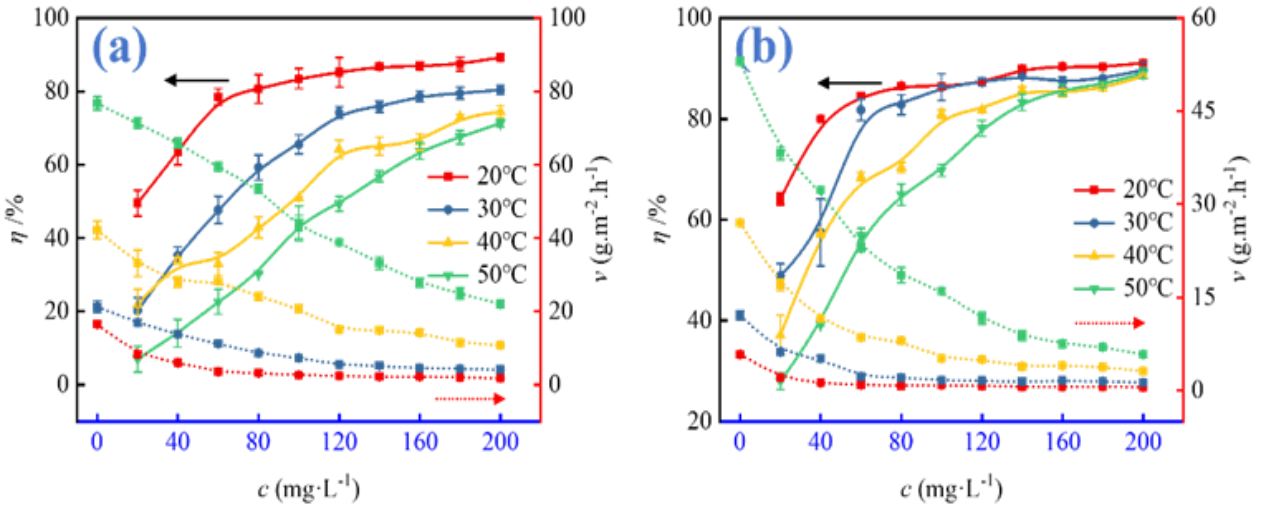

Fig. 3: Corrosion rate and inhibition efficiency in 0.5 M H_2SO_4 (a) and 1 M HCl (b) containing different concentrations of PURME.

repulsive forces on the CRS surface intensify, causing the slopes of both the correlation coefficients and regression lines approach unity more closely at lower temperatures, indicating enhanced PURME adsorption under these conditions. With increasing temperature, the intermolecular repulsive forces on the CRS surface intensify, causing the slopes of both the correlation coefficients and regression lines to deviate progressively from unity.[35] However, Fig. 4(b1) shows that in HCl, PURME adsorption follows the Langmuir adsorption isotherm at any temperature The Freundlich adsorption models are shown in Fig. 4(a2) and 4(b2), respectively. When $0<n<1$, corrosion inhibitors can be adsorbed on metal surfaces more readily. When $n>1$, adsorption is more difficult.[36] The values of n are less than 1 except at 50 °C in sulfuric acid, which indicates that the low temperature can be favorable for adsorption. The Temkin adsorption models are shown in Fig. 4(a3) and (b3), respectively, in which f is greater than 0, which indicates that the corrosion inhibitor molecules are repulsive to each other.[37]

Whether in H_2SO_4 or HCl solution, the adsorption equilibrium constants (K), obtained from these three adsorption models, show a tendency of decreasing gradually with increasing temperature, indicating that PURME can adsorb better at low temperatures and show better corrosion inhibition performance.[37]

$$\frac{c}{\theta} = \frac{1}{K} + c \tag{3}$$

$$\ln\theta = \ln K + n\ln c \tag{4}$$

$$\theta = \left(\frac{1}{f}\right)\ln c + \left(\frac{1}{f}\right)\ln \tag{5}$$

3.5 Corrosion kinetic of PURME on CRS's surface

The corrosion behavior can be effectively described by both the Arrhenius equation and transition state theory, with the corresponding mathematical expressions presented as follows Eq. (6-7)[38,39]:

$$\ln v = \frac{-\mathrm{Ea}}{\mathrm{RT}} + \ln \mathrm{A} \tag{6}$$

$$\ln\left(\frac{\mathrm{v}}{\mathrm{T}}\right) = \ln\left(\frac{\mathrm{R}}{\mathrm{Nh}}\right) + \frac{\Delta \mathrm{S_a}}{\mathrm{R}} - \frac{\Delta \mathrm{H_a}}{\mathrm{RT}} \tag{7}$$

Ea is the apparent activation energy (kJ·mol^{-1}), A is the index factor (g·(m^2·h)$^{-1}$). ΔH_a is activation enthalpy (kJ·mol^{-1}), ΔS_a is activation entropy (J·(mol·K)$^{-1}$), N is Avogadro's constant (6.02×10^{23} mol^{-1}), and h is Planck's constant (6.626×10^{-34} J·s).

Fig. 4 (a4, a5) and 4 (b4, b5) show the fitted plots of the two. The fitted equations demonstrate excellent linear correlations in both acidic media, as evidenced by correlation coefficients approaching 1. The resulting variation curves for the corrosion kinetic parameters (Ea-c, ln$A$-c, ΔH_a-c, ΔS_a-c) are presented in Fig. 4a(6) and 4b(6). The observed Ea values increase first, which suggests that PURME adsorbs first on the surface of the steel sheet by electrostatic action, *i.e.*, physical adsorption.[36] Subsequent decrease in Ea value indicates chemisorption at the metal-solution interface.

A is related to the number of active sites, the greater the density of active sites, the higher the frequency of collisions. In both acidic media, ln$A$ maintains near-constant values, demonstrating that A remains essentially unchanged. This observation suggests that the surface density of active sites on CRS remains largely unaffected following the introduction of PURME, indicating that the inhibitor's primary mechanism does not involve significant alteration of the surface active site distribution.[40] ΔH_a confirms the endothermic nature of the corrosion process, demonstrating that significant thermal energy absorption from the surrounding environment is required for the reaction to proceed. Notably, ΔS_a exhibits a characteristic transition: initially negative, gradually increasing to positive values, and subsequently returning to negative values. This behavior reflects the system's initial low degree of freedom, followed by increased disorder as PURME molecules compete with corrosion species for surface active sites. As the adsorption process progresses, the system reaches

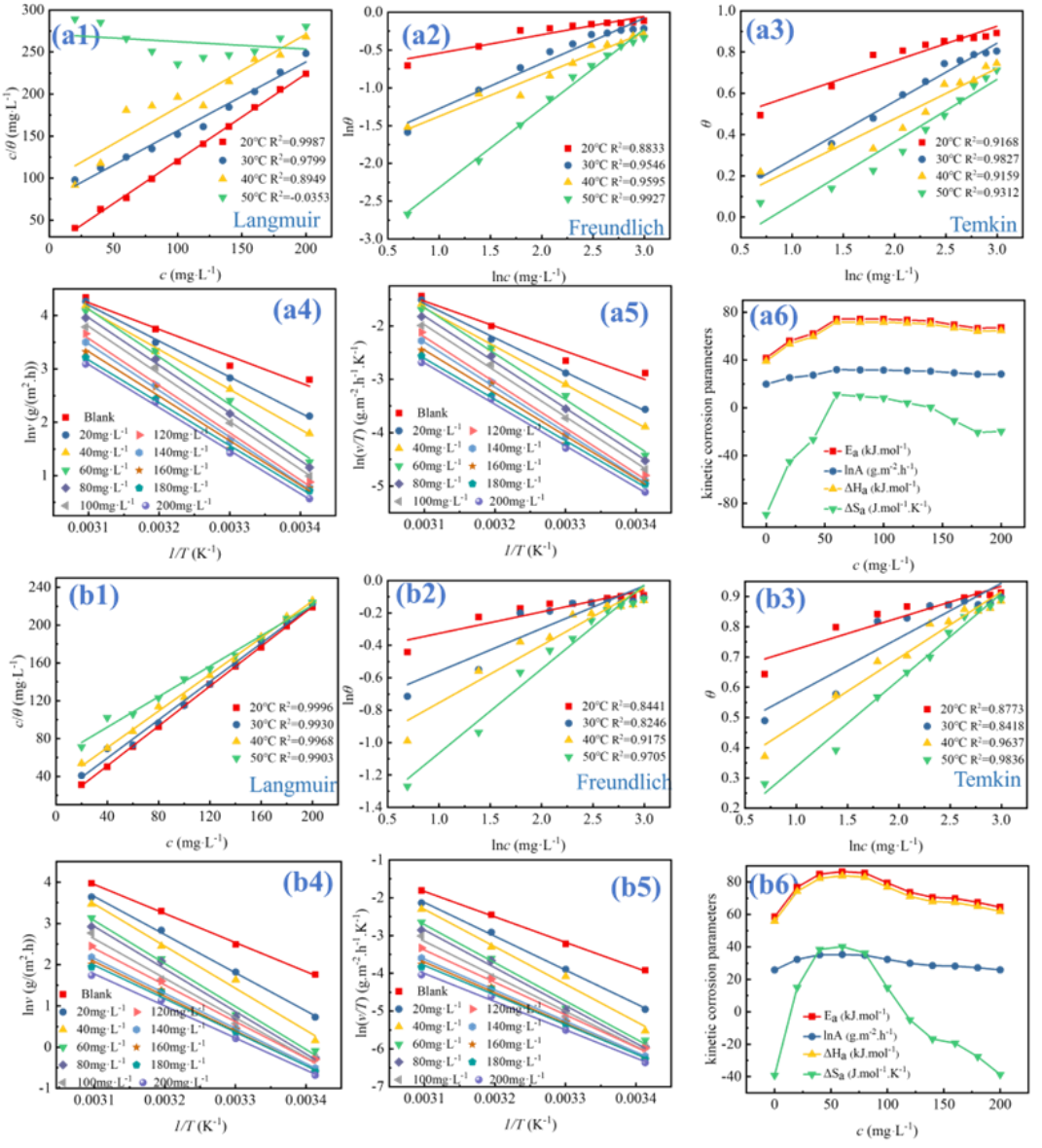

Fig. 4: The Langmuir (1), Freundlich (2) and Temkin adsorption isotherm (3), corrosion rate related Arrhenius (4) and transition state (5) fitting lines and curves of the corrosion kinetic parameters (6) in 0.5 M H_2SO_4 (a)and in 1 M HCl (b).

Table 1: The parameters of the fitted straight line.

Acid	T (°C)	Langmuir		Freundlich		Temkin	
		slope	K	n	K	f	K
H_2SO_4	20	1.029	0.055	0.243	0.456	1.073	12.141
	30	0.818	0.013	0.599	0.153	0.999	0.985
	40	0.871	0.010	0.554	0.145	0.997	0.944
	50	-0.088	0.004	1.049	0.034	0.929	0.450
HCl	20	1.053	0.110	0.133	0.632	1.610	1.982
	30	1.014	0.053	0.264	0.438	2.508	1.637
	40	0.969	0.032	0.355	0.330	3.880	1.387
	50	0.806	0.017	0.520	0.205	19.531	1.073

surface saturation, resulting in decreased disorder, as evidenced by the final negative ΔS_a values.

3.6 Analysis of kinetic potential polarization curves

In order to clarify the electrochemical mechanism, kinetic potential polarization curves were systematically analyzed. Fig. 5a(1) and 5b(1) illustrate the kinetic potential polarization curves obtained for various concentrations of PURME in acidic solutions at 20 ℃. Tafel curves indicate that the corrosion current density gradually decreases as the concentration of PURME increases, and this decrease is more significant in the cathodic region under both acidic environments. In addition, the cathodic polarization curves remain basically parallel to those of the blank solution, with their slopes remaining essentially unchanged, and there is clearly a well-defined Tafel region, indicating that the corrosion mechanism has not been altered.[40]

It is noteworthy that in HCl solution, the anodic Tafel curve exhibits a distinct morphological change at elevated concentrations of the corrosion inhibitor. Generally, this curve can be divided between adsorption part, adsorption plateau part and desorption part,[42] but the concentration of PURME is larger, so the adsorption plateau part is not very obvious. In the adsorption part, as the electrode potential and corrosion current density increase, a substantial number of PURME molecules adsorb onto the electrode surface, thereby impeding the anodic dissolution process of the CRS electrode. Upon reaching a critical corrosion potential of -0.26 V, complete desorption of PURME molecules from the electrode surface occurs. Beyond this threshold potential, the anodic polarization curve exhibits near-complete overlap with the blank solution, demonstrating the absence of corrosion inhibition effects. In contrast, when PURME's concentration is 20 $mg \cdot L^{-1}$, no distinct characteristic sections appear, suggesting that at lower concentrations, the adsorption equilibrium of PURME in HCl solution is not disrupted by the adsorption-desorption process. As summarized in Table 2, i_{corr} shows a concentration-dependent decrease, declining from 401 to 19 $\mu A \cdot cm^{-2}$ in H_2SO_4 and from 741 to 60 $\mu A \cdot cm^{-2}$ in HCl solutions with increasing PURME concentration. The inhibition efficiency (η_P) derived from polarization curve analysis, calculated using Eq. (8),[43] yields values of 95.3% and 91.9% in the respective acidic media. These quantitative results demonstrate that PURME exhibits enhanced corrosion inhibition performance at elevated concentrations. In both acidic environments, the absolute value of the corrosion potential difference E is less than 85mv, this suggests that PURME is a hybrid corrosion inhibitor that mainly inhibits cathodic reactions.[44]

Some scholars have proposed to use the anodic reaction coefficient (f_a) and the cathodic reaction coefficient (f_c)[42] to express the effect of corrosion inhibitors on the cathodic and anodic reactions of the corrosion process, and these two coefficients are calculated by Eq. (9,10).[44] In H_2SO_4 solution, at PURME concentrations of 0, 20, and 100 $mg \cdot L^{-1}$, both f_a and $f_c < 1$, suggesting that the electrochemical mechanism at this time was activity blocking at PURME concentrations of 200 $mg \cdot L^{-1}$, $f_a > 1$ and $f_c < 1$ indicate that the cathodic mechanism remains unchanged, but the anodic mechanism is mainly electrocatalytic, which means that the corrosion inhibitor promotes the cathodic reaction at this potential. At f_a and $f_c < 1$ in HCl solution, the electrochemical mechanism is active site blocking.[47]

The polarization resistance (R_P) was calculated according to Eq. (11).[48,49] In both acidic environments, the R_P demonstrated a progressive increase. It is demonstrated that as the concentration of PURME increases, the surface adsorption film layer will become thicker, and the protection of the metal will be more thorough.

$$\eta_P = \frac{i_{corr(0)} - i_{corr(inh)}}{i_{corr(0)}} \times 100\% \quad (8)$$

$$f_a = \left(\frac{i_{corr}^{inh}}{i_{corr}^{0}}\right) \exp \frac{E_{corr}^{0} - E_{corr}^{inh}}{b_a} \quad (9)$$

$$f_c = \left(\frac{i_{corr}^{inh}}{i_{corr}^{0}}\right) \exp \frac{E_{corr}^{inh} - E_{corr}^{0}}{b_c} \quad (10)$$

$$R_P = \frac{b_a b_c}{2.303 i_{corr}(b_a + b_c)} \quad (11)$$

Where $i_{corr(0)}$ and $i_{corr(inh)}$are the corrosion current densities without and with PURME, respectively.

3.7 EIS analysis

Fig. 5(a2) and Fig. (b2) show the EIS measurements for two acidic solutions containing different concentrations of PURME. The Nyquist plots in both systems consistently display a single capacitive semicircle, with their characteristic shapes remaining essentially unaltered. This indicates that the electrochemical corrosion process in both acidic media is primarily dictated by the charge-transfer at the electrode-electrolyte interface. Even with the incorporation of PURME, the fundamental corrosion mechanism remains unaltered, indicating that the inhibitor primarily functions through surface adsorption rather than altering the intrinsic corrosion pathway.

The capacitance arc is not a perfect semicircle, can be attributed to several factors including surface roughness-induced diffusion effects, non-uniform adsorption distribution.[50] and heterogeneous diffusion processes occurring during the progressive metal corrosion.[51] In the absence of PURME, the Nyquist plot in H_2SO_4 solution exhibits a significantly smaller radius compared to that observed in HCl solution, indicating that the working electrode undergoes more severe corrosion in H_2SO_4 solution. Fig. 5(a3) and Fig. 5(b3) present the Bode plots. From these plots, it is evident that as the PURME concentration increases, the absolute modulus values in the low-frequency region also

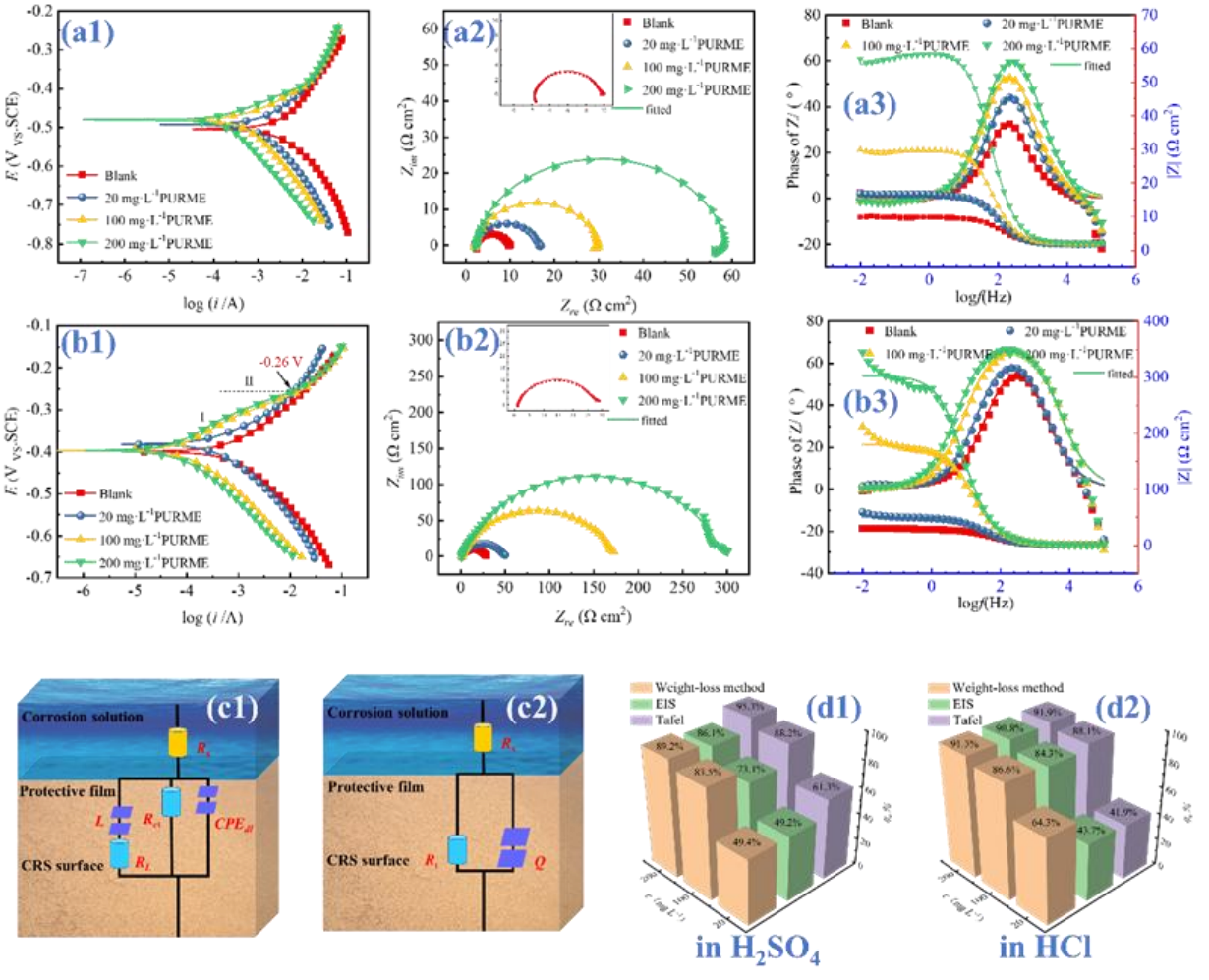

Fig. 5: Potential dynamic polarization curves (1) Nyquist plots (2) Bode plots (3) for CRS in 0.5 M H_2SO_4 (a)and in 1 M HCl (b) with different concentrations of PURME at 20 ℃. The corresponding equivalent circuit graphs (c), inhibition efficiency (d).

Table 2: Potential dynamic polarization parameters.

Acid	PURME	E_{corr}	i_{corr}	$-b_c$	b_a	R_p	f_c	f_a	f_a/f_c	η_p
	(mg·L)	(mV vs. SCE)	(μA·cm^{-2})	(mV·dec^{-1})	(mV·dec^{-1})	Ω·cm^2	-	-	-	(%)
H_2SO_4	0	-504	401	134	171	81.4	-	-	-	-
	20	-492	155	161	172	233.0	0.36	0.83	2.29	61.3
	100	-480	47	131	62	388.8	0.08	0.97	12.24	88.3
	200	-480	19	125	52	839.3	0.03	1.02	34.27	95.3
HCl	0	-420	741	115	101	31.5	-	-	-	-
	20	-403	430	139	94	56.6	0.37	0.77	2.11	41.9
	100	-400	88	109	68	206.6	0.05	0.99	20.99	88.1
	200	-397	60	109	67	300.3	0.03	0.99	32.70	91.9

increase, suggesting that the corrosion inhibition effect of PURME improves with concentration. The phase angle plots show a distinct phase peak in the mid-frequency range ($\log f$ = 2-4), indicating that there is a time constant in the EIS.[52]

The equivalent circuit diagram $R_s(QR_t(LR_L))$,[53] (Fig. 5(c1)) was used to fit the EIS data for the 200 mg·L^{-1} PURME concentration in sulfuric acid, while ($R_s(QR_t)$[54] (Fig. 5(c2)) was used for the other concentrations. R_s is solution resistance, R_t is charge-transfer resistance, Q is constant phase angle element, and L is inductor, which is related to the inductive behavior in the circuit. The relevant data are presented in Table 3. The fitted chi-square (χ^2) value is small,[55] which indicates that the chosen fitted circuit diagram fits the experimental data very well. R_t's value increases gradually with PURME's concentration. R_t increases from 7.4 Ω·cm^2 to 56.7 Ω·cm^2 in H_2SO_4 and 47.8 Ω·cm^2 to 302.8 Ω·cm^2 in HCl, showing that the charge transfer process is effectively impeded. Calculated from Eq. (12),[56] the corrosion inhibition efficiency(η_R) is the highest among these two acids at 86.1% and 90.8%, respectively.

$$\eta_R = \frac{R_{t(inh)} - R_{t(0)}}{R_{t(inh)}} \times 100\% \quad (12)$$

$R_{t(0)}$ and $R_{t(inh)}$ are the charge transfer resistances without and with PURME, respectively.

Using Eq. (13)[57] to calculate the double-layer capacitance (C_{dl}). According to Eq. (14),[55] C_{dl} is related to the protective film thickness.

$$C_{dl} = Q \times (2\pi f_{max})^{n-1} \quad (13)$$

f_{max} denotes the maximum eigenfrequency (Hz) on the imaginary axis of the Nyquist spectrum.

$$C_{dl} = \frac{\varepsilon^0 \varepsilon}{d} S \quad (14)$$

where ε^0 is vacuum dielectric constant,[37] ε is double layer dielectric constant, d is the protective film thickness, and S is the effective surface area of the electrode. The results indicated that C_{dl} decreases with increasing PURME concentration. With the addition of PURME, a protective film forms on the surface of CRS, replacing adsorbed water molecules. With the increase of the concentration of PURME, the growth of the protective film will correspondingly reduce the surface area of the working electrode exposed to the corrosive medium, thus significantly inhibiting corrosion.

3.8 XPS surface analysis

The XPS profile of CRS in H_2SO_4 and HCl media is shown in Fig. 6. The presence of O 1s, N 1s, and C 1s peaks from PURME in the full spectrum proves it is adsorbed on CRS's surface.

Fig. 6(a2) and 6(b2) presents the Fe 2p spectrum. Two distinct peaks were observed in both acid media, one peak corresponding to the 2p$^{3/2}$ XPS energy spectrum of iron at 711.0 eV and the other to the 2p$^{1/2}$ XPS energy spectrum of iron at 724.7 eV. But in the sulfuric acid, the peaks with binding energies of 710.6, 712.3, 718.8, and 725.1 eV correspond to Fe_2O_3, $FeSO_4$, FeO, and $Fe(H_2O)$,[58] respectively. And in HCl medium, The peaks with binding energies of 711.4, 713.8, 724.3, and 726.2 eV correspond to Fe_2O_3, $FeCl_3$, FeOOH, and $Fe(H_2O)$, respectively. Among them, Fe_2O_3, FeO, FeOOH, and $Fe(H_2O)$ may be the substances generated from the combination of CRS surface with water and oxygen, and $FeSO_4$ and $FeCl_3$ are the corrosion products in acid medium, respectively.

The spectra of C 1s and O 1s are shown in Fig. 6(a3, b3) and (a4, b4), respectively. The spectra of C 1s and O 1s in these two acidic media appeared almost the same results. In the carbon spectra, the peaks with binding energies of 284.8, 286.2, and 288.4 eV corresponded to C-C/C-H, C-OH/C-O-C, and C-O,[52] respectively. In the oxygen spectra, the peaks with binding energies of 529, and 531 eV corresponded to the substances of metal oxides and oxygen in adsorbed water.[59,60].

The spectra of N 1s are shown in Fig. 6(a5, b5). As can be seen from the figure, the peaks with binding energies of 399.8 and 400.4 eV in H_2SO_4 medium correspond to C-N and C-N$^+$, respectively; the peak with binding energy of 399.9 eV in HCl medium corresponds to C-N.[61] From the above XPS spectra. There are functional groups such as C-C/C-H, C-OH/C-O-C, C-O, C-N on CRS.

3.9 Contact angle, AFM and TOF-SIMS analysis

The upper left corner of Fig. 7 (a1-e1) shows the contact angle plots obtained by testing CRS under different conditions The freshly polished steel sheet exhibits a contact angle of 79.61°, indicating good hydrophilicity and ease of wettability. Upon immersion in pure acids, the contact angle decreases to 61.58° and 75.46°, respectively. This reduction signifies enhanced hydrophilicity of the surface, making it more susceptible to further corrosion in the acidic medium. However, when 200 mg·L^{-1} PURME is added, the contact angle increases significantly to 105.39° and 125.20°, respectively. The notable increase in contact angle values unambiguously demonstrates that PURME efficiently establishes a physical barrier. This barrier enhances the hydrophobicity of the surface while preventing corrosive liquids from coming into direct contact with the CRS.[62]

AFM, as a powerful surface characterization technique, has been extensively employed for microstructural analysis and surface roughness quantification of various materials. Fig. 7(a) presents the 3D-AFM topography of the CRS surface immediately following the polishing process, demonstrating a relatively uniform surface morphology with characteristic polishing-induced striations. Fig. 7(b) and (c), as well as (d) and (e), depict the 3D-AFM images of CRS immersed in H_2SO_4 and HCl media, with and without 200 mg L^{-1} PURME at 20 °C respectively. The images illustrate significant surface corrosion in both acid media, characterized by pronounced undulations. However, after the addition of PURME, the CRS

Table 3: EIS fitted parameters.

Acid	PURME (mg/L)	R_s ($\Omega \cdot cm^2$)	n	R_t ($\Omega \cdot cm^2$)	Q ($\mu\Omega \cdot S^a \cdot cm^{-2}$)	f_{max} (Hz)	L H	R_L ($\Omega \cdot cm^2$)	C_{dl} ($\mu F/cm^2$)	X^2	η_R (%)
H_2SO_4	0	2.3	0.9043	7.4	446	98	-	-	241.3	5.7×10^{-3}	--
	20	2.0	0.8913	14.6	310	68	-	-	160.5	3.2×10^{-3}	49.2
	100	2.0	0.9026	27.6	209	46	-	-	120.3	2.8×10^{-3}	73.1
	200	2.1	0.8936	56.7	124	38	1998	855.7	69.2	1.8×10^{-3}	86.1
HCl	0	1.12	0.8330	27.9	355	38	-	-	142.3	1.1×10^{-2}	--
	20	1.16	0.8262	49.6	347	21	-	-	148.5	9.9×10^{-3}	43.7
	100	1.01	0.8270	178.4	186	10	-	-	90.9	1.6×10^{-2}	84.3
	200	1.07	0.8240	302.8	175	6	-	-	92.4	1.2×10^{-2}	90.8

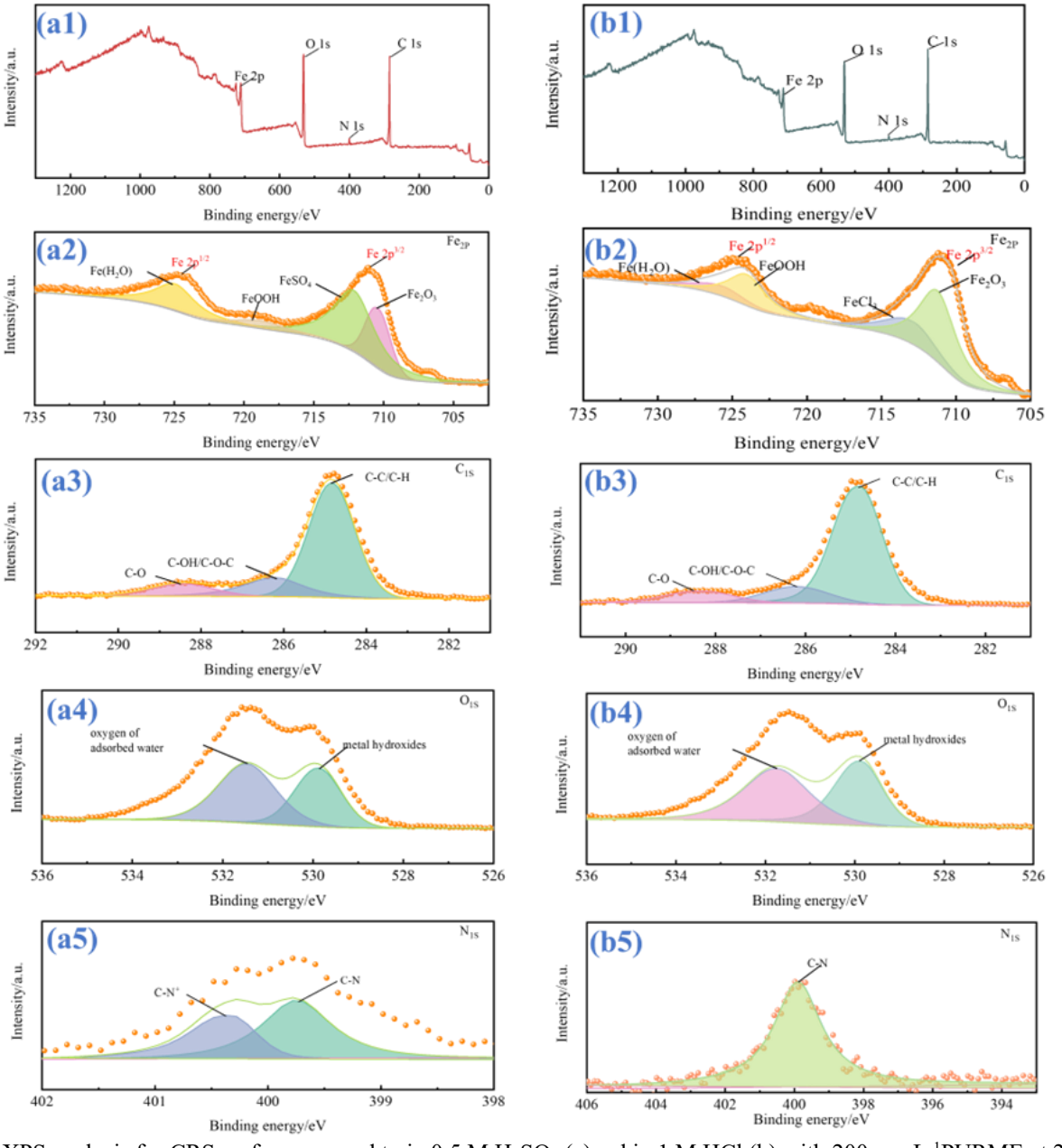

Fig. 6: XPS analysis for CRS surface exposed to in 0.5 M H_2SO_4 (a)and in 1 M HCl (b) with 200 mg·L^{-1}PURME at 20 °C.

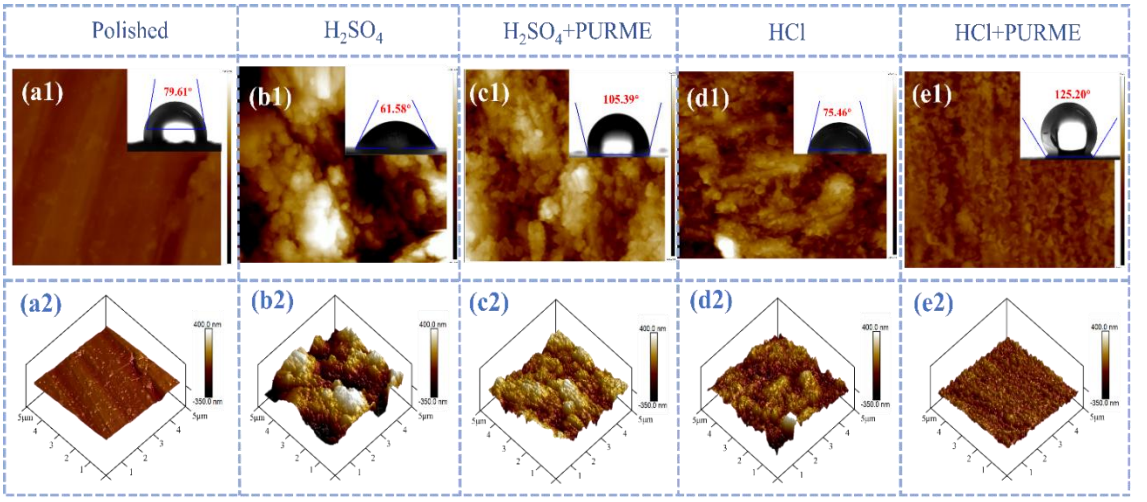

Fig. 7: AFM 3D micrographs and contact angle (1) (2) of CRS specimens: (a) Polished; (b) after immersion in 0.5M H_2SO_4 solution; (c) after immersion in 0.5M H_2SO_4 solution with 200 mg L^{-1} PURME; (d) after immersion in 1M HCl solution; (e) after immersion in 1M HCl solution with 200 mg L^{-1} PURME;

Table 4: The AFM roughness parameters of CRS surface.

	R_q/nm	R_a/nm	R_{max}/nm
Before immersion	19.5	15.1	180
H_2SO_4	189	152	1411
H_2SO_4+PURME	118	97.1	750
HCl	91.6	71.6	832
HCl+PURME	40.4	31.8	302

surface immediately following the polishing process, demonstrating a relatively uniform surface morphology with characteristic polishing-induced striations. Fig. 7(b) and (c), as well as (d) and (e), depict the 3D-AFM images of CRS immersed in H_2SO_4 and HCl media, with and without 200 mg L^{-1} PURME at 20 °C respectively. The images illustrate significant surface corrosion in both acid media, characterized by pronounced undulations. However, after the addition of PURME, the CRS surface became noticeably smoother, with reduced undulations, demonstrating the effective corrosion inhibition provided by PURME.[63] Table 4 presents surface roughness parameters obtained from AFM measurements These parameters serve as important indicators for assessing the degree of corrosion on metal surfaces. A smaller surface roughness value suggests a more even and smoother surface. After the addition of PURME, all surface roughness parameters are significantly reduced, indicating that PURME effectively inhibits corrosion on the CRS surface.

Fig. 8 shows the mass spectra and corresponding images of CRS surface fragments in both H_2SO_4 and HCl, respectively. As can be seen from the test results, a large number of O, N, P heteroatoms were detected in these fragments, indicating that PURME can combine with Fe to form complexes adsorbed on the surface. Ionic fragments such as $-CH_3$, $-C_2H_5$, $-C_3H_5$, $-C_4H_5$, $-C_4H_9$, $-C_6H_5$ were also detected, suggesting that there are unsaturated functional groups such as alkyl, olefinic and aromatic groups in PURME.[35] The presence of these heteroatoms and unsaturated functional groups further confirms that PURME can inhibit corrosion by adsorbing uniformly and in large quantities to form adsorbent films on surfaces.[36]

3.10 Quantum chemical calculations of chenodeoxycholic acid and linolenic acid

QC is used to further calculate and analyze the adsorption mechanism of these two substances. Combined with the literature and LC-MS results, chenodeoxycholic acid and linolenic acid are selected to carry out QC and molecular dynamics simulation studies on these two substances. Given that both H_2SO_4 and HCl represent strongly acidic environments, it is essential to consider the protonation effects on corrosion inhibitor molecules and their subsequent influence on inhibition efficiency. Fig. 9 is a plot of the results of QC calculations for chenodeoxycholic acid and linolenic acids and their protonated molecules. Chenodeoxycholic acid before and after the protonation of HOMO are in the ring, while LUMO is in the carboxyl group in the tail of the molecule. Linolenic acid before and after the protonation of HOMO are in the C = C, while LUMO is in the -COOH, indicating that the C-C, C = C, -COOH can accept Fe's electrons to form a metal feedback bond.[64] As a result, it adsorbs better to the surface. Eq. (15-18) are used to calculate the γ (overall hardness), s (overall softness), β (absolute electronegativity) and ΔN (Number of electrons transferred from the corrosion inhibitor to the metal surface).[65] The relevant values obtained are listed in Table 5. The subversive difference between the Fe surface and the corrosion inhibitor molecules will result in the transfer of electrons to the electronegative one until the chemical potentials are the same. When $\Delta N > 0$, electrons are transferred from the corrosion inhibitor molecules to the Fe surface and vice

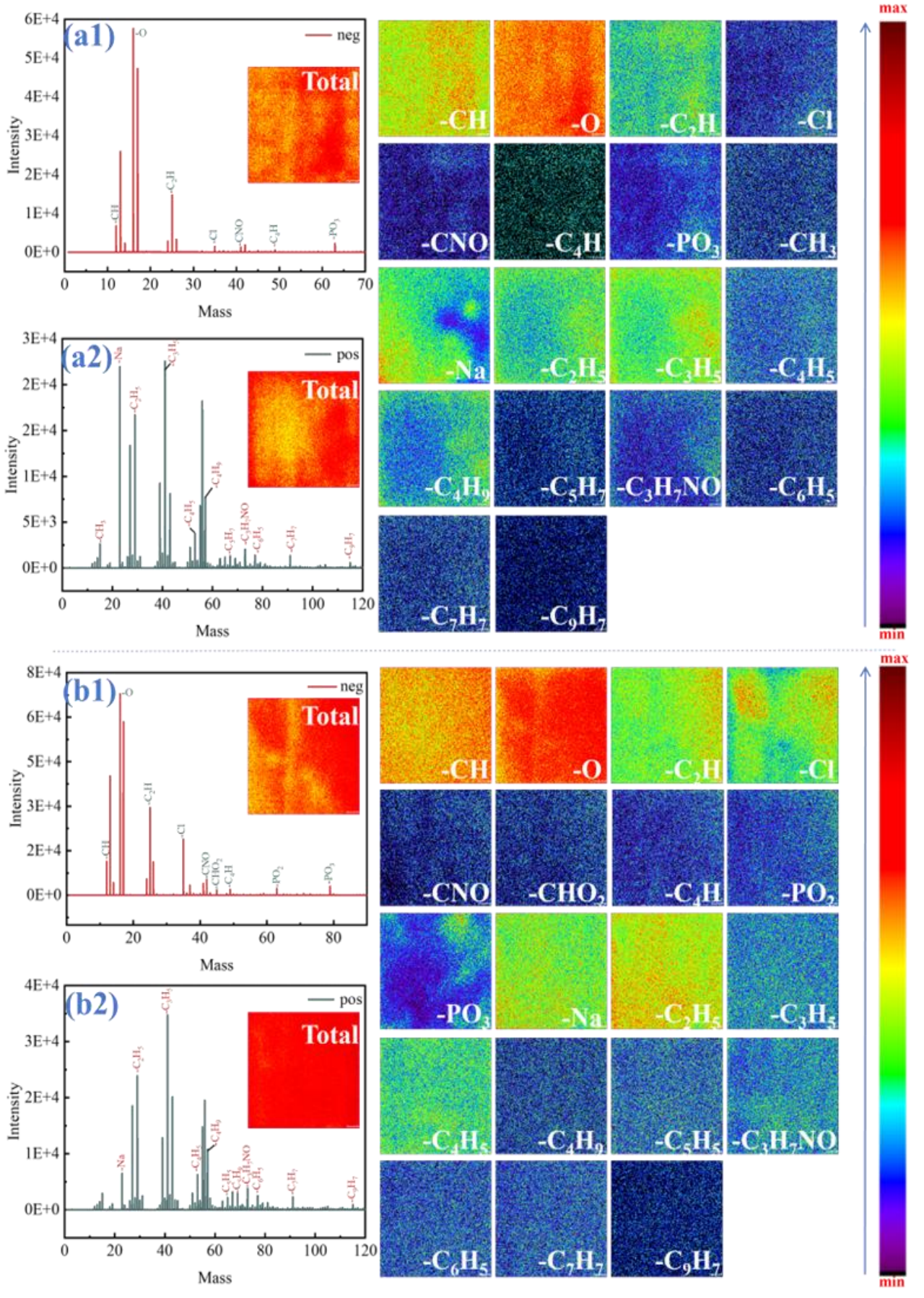

Fig. 8: TOF-SIMS of negative and positive ion spectrogram and the corresponding fragments for CRS after immersing in 0.5M H_2SO_4(a) and 1.0 M HCl(b) solution with 200 mg L^{-1} PURME for 6 h in 20 °C.

versa.[66] If ΔN < 3.6, it indicates that corrosion inhibition increases with the ability of the molecule to give electrons on the metal surface.[67] The calculated values of Δ*N* are all greater than 0 and less than 3.6, which indicate that the molecules are combined with Fe in the form of ligand bonding. The above data indicate that the protonated corrosion inhibitor molecules can be better combined with Fe, which will show better corrosion inhibition performance.

$$\gamma = \frac{\Delta E}{2} \tag{15}$$

$$= \frac{1}{\gamma} \tag{16}$$

$$\beta = -\frac{E_{\mathrm{HOMO}} + E_{\mathrm{LUMO}}}{2} \tag{17}$$

$$\Delta N = \frac{\beta_{\mathrm{Fe}} - \beta_{\mathrm{inh}}}{2(\gamma_{\mathrm{Fe}} - \gamma_{\mathrm{inh}})} \tag{18}$$

$$f_{\mathrm{i}}(r)^{+} = q_{\mathrm{i}}(N+1) - q_{\mathrm{i}}\,(N) \tag{19}$$

$$f_{\mathrm{i}}(r)^{-} = q_{\mathrm{i}}(N) - q_{\mathrm{i}}\,(N-1) \tag{20}$$

β_{Fe} and γ_{Fe} values of 7 eV and 0 Ev,[70] respectively.

The Fukui index enables a better observation of local site selectivity. $f(\mathrm{r})^{+}$ and $f(\mathrm{r})^{-}$ functions are given by Eq. (19,20).[68,69] Higher $f(\mathrm{r})^{+}$values indicate that the atoms are accepts more electrons, while higher $f(\mathrm{r})^{-}$ values indicate that the atom loses more electrons, the electrophilic/nucleophilic centers of chenodeoxycholic acid and its protonated molecules are at -COOH and -OH, respectively and the electrophilic/nucleophilic centers of linolenic acid in and its protonated molecules are at C=C and -COOH, respectively. It is through these sites that the corrosion inhibitor adsorbs and binds better to the metal surface. The tighter the adsorption, the better the corrosion inhibition.

3.11 MD simulations

Adsorption properties of chenodeoxycholic acid, linolenic acid and their corresponding protonated forms on Fe (110) surfaces studied by MD simulation. (in Fig. 10). These molecules adsorb through multiple different adsorption sites and can effectively cover, exhibiting good corrosion inhibition performance.

By calculating the binding energy E_{int}, the adsorption capacity and inhibition of different molecules can be judged. when the value of E_{int} is negative, it results that the molecular adsorption on the Fe (110) surface occurs spontaneously, where a more negative adsorption energy value corresponds to greater system stability and enhanced corrosion inhibition efficiency.[71] The adsorption capacity of different molecules can be determined from the simulated E_{int} values of chenodeoxycholic acid and linolenic acid and their protonated molecules in different acidic environments. It can be seen that the absolute E_{int} values of phenol deoxycholic acid and its protonated molecules are greater, suggesting that their adsorption on the Fe(110) surface is more stable and firmer.

The radial distribution function (RDF) can be used to determine the bonding information of molecules in the plane of Fe(110). When the distance between two particles(r) is greater than 3.5 Å, it indicates physical bonding, involving only Coulombic and van der Waals forces, and when r is less than 3.5 Å, covalent bonding. If the g(r) value peaks within 3.5 Å, it indicates the presence of chemical adsorption, with an excellent chemisorption ability.[72] It is clear that the g(r) values of Fe-O for individual molecules peaked within 3.5 Å and still peaked after 3.5 Å. This is strong evidence that the adsorption of molecules of chenodeoxycholic acid and linolenic acid and their protonated molecules on the Fe(110)'s surface in different acidic environments is a combination of both chemical adsorption and physisorption. The synergistic effect between chemical adsorption and physisorption enhances the binding strength and packing density of these molecules on the steel surface, thereby achieving highly efficient inhibition.

3.12 Corrosion protection mechanism of PURME in sulfuric and hydrochloric acid media

H_2SO_4 and HCl are strong acid, which are intensely corrosive, and both can be completely ionized in aqueous solution to produce H^+ and SO_4^{2-} or Cl^-. The cathode of iron in H_2SO_4/HCl solution produces a large number of bubbles and hydrogen precipitation reaction occurs as follows Eq. (21)[73,74]:

$$2H^{+}+2e^{-}\rightarrow H_2 \tag{21}$$

Iron undergoes a corrosion reaction at the anode in a sulfuric/hydrochloric acid solution by the following process Eq. (22-24):

$$Fe+H^{+}\rightarrow(FeH^{+})_{ads} \tag{22}$$

$$(FeH^{+})_{ads}+e^{-}\rightarrow(FeH)_{ads} \tag{23}$$

$$(FeH)_{ads}+H^{+}+e^{-}\rightarrow Fe+H_2 \tag{24}$$

Total process Eq. (25):

$$Fe\rightarrow Fe^{2+}+2e^{-} \tag{25}$$

The adsorption process of SO_4^{2-} on Fe Eq. (26-29):

$$Fe+SO_4^{2-}\rightarrow(FeSO_4^{2-})_{ads} \tag{26}$$

$$(FeSO_4^{2-})_{ad}\rightarrow(FeSO_4)_{ads}+2e^{-} \tag{27}$$

$$(FeSO_4)_{ads}\rightarrow FeSO_4 \tag{28}$$

$$FeSO_4\rightarrow Fe^{2+}+SO_4^{2-} \tag{29}$$

The adsorption process of Cl^- on Fe Eq. (30-33):

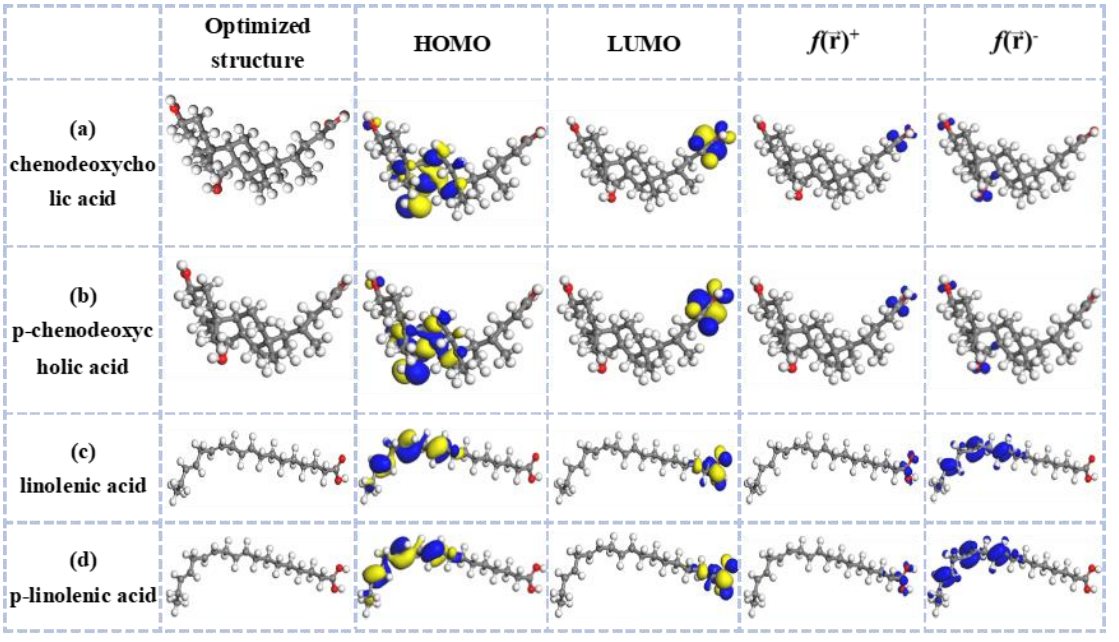

Fig. 9: QC calculations of chenodeoxycholic acid and linolenic acid as well as their protonated molecules.

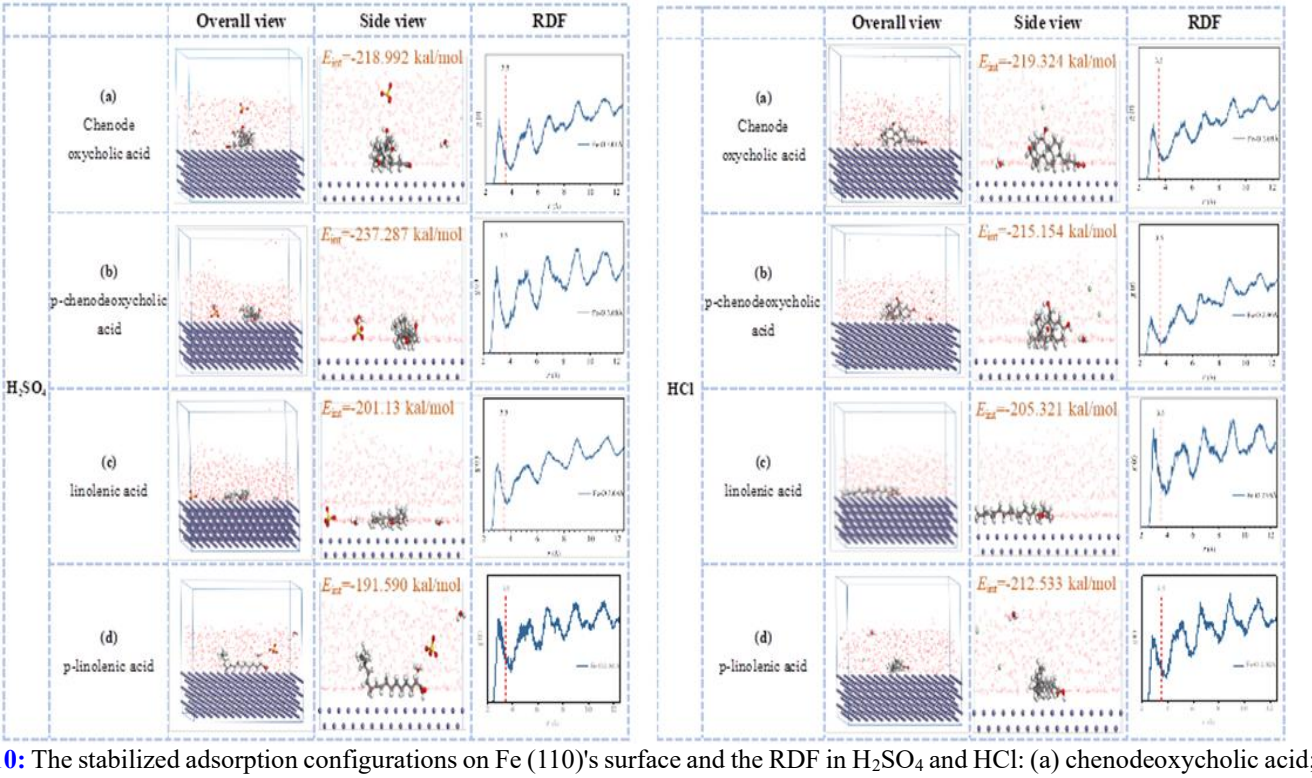

Fig. 10: The stabilized adsorption configurations on Fe (110)'s surface and the RDF in H_2SO_4 and HCl: (a) chenodeoxycholic acid;(b) p-chenodeoxycholic acid; (c) linolenic acid; (d) p-linolenic acid.

Table 5: QC parameters.

Molecule	E_{HOMO}(eV)	E_{LUMO}(eV)	ΔE (eV)	γ	s	β	ΔN
chenodeoxycholic acid	-5.864	-0.852	5.012	2.506	0.399	3.358	0.727
p-chenodeoxycholic acid	-5.908	-3.266	2.642	1.321	0.757	4.587	0.913
linolenic acid	-5.543	-1.210	4.333	2.166	0.462	3.376	0.836
p-linolenic acid	-5.559	-3.336	2.223	1.111	0.900	4.447	1.148

$$Fe + Cl^- \rightarrow (FeCl^-)_{ads} \quad (30)$$

$$(FeCl^-)_{ads} \rightarrow (FeCl)_{ads} + e^- \quad (31)$$

$$(FeCl)_{ads} \rightarrow FeCl^+ + e^- \quad (32)$$

$$FeCl^+ \rightarrow Fe^{2+} + Cl \quad (33)$$

PURME undergoes protonation and is able to adsorb well on the CRS surface in the following process Eq. (34):

$$PURME + xH^+ \rightarrow PURMEHx^{x+} \quad (34)$$

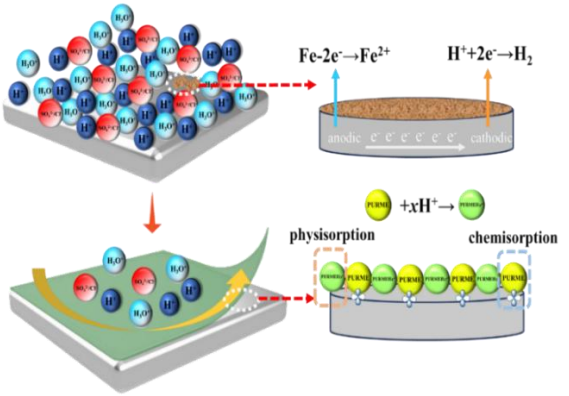

Fig. 11: Adsorption schematic diagram.

Generally speaking, the effect of corrosion prevention can be achieved by both physical isolation and chemical passivation (*e.g.*, formation of dense oxide film, etc.).[75] As evident from the aforementioned reaction, the acidic medium dissociates in water to form H^+ and SO_4^{2-}/Cl^- ions, which adsorb onto the CRS surface, thereby inducing corrosion. The positively charged $PURMEH_x^{x+}$ cations electrostatically interact with the pre-adsorbed SO_4^{2-}/Cl^- anions on the CRS surface, forming a physical adsorption layer. PURME is a mixture that contain a large number of polar functional groups (*e.g.*, -COOH, -C=O, -C-N, etc.) and heteroatoms (*e.g.*, O, N, P, etc.). They have many lone pairs of electrons, which can combine with the empty orbitals on Fe 3d to form an insoluble complex, which can be well adsorbed on the surface of the steel sheet, which is chemisorption. The synergistic interaction between physical adsorption and chemical adsorption promotes the formation of a compact protective film on the surface of CRS. The mechanism of action of PURME can be referenced in Fig. 11. This film effectively mitigates the corrosive effects induced by H^+ ions and SO_4^{2-}/Cl^- anions, leading to a substantial improvement in corrosion inhibition efficiency.

4. Conclusion

The following conclusions are drawn from this study:

(1) The best performance was achieved at 20 ℃ and a PURME concentration of 200 $mg \cdot L^{-1}$, with corrosion inhibition efficiencies of 89.25% and 91.28% in H_2SO_4 and HCl acids, respectively. The adsorption behavior of PURME on the CRS surface follows Langmuir, Freundlich, and Temkin adsorption isotherm models.

(2) PURME functions as a mixed-type corrosion inhibitor with predominant cathodic inhibition characteristics. As the concentration of PURME increases, the charge transfer process at the metal-liquid interface is effectively hindered, resulting in efficient inhibition properties.

(3) FTIR and LC-MS indicate that PURME contains polar functional groups such as N-H/O-H, C-H, C=O/C=C, $-CH_3$, -C-O-. AFM, contact angle all indicate that PURME can effectively prevent the corrosion. TOF-SIMS and XPS results are able to show that these polar functional groups can form adsorption films on the CRS surface and thus inhibit corrosion.

(4) QC shows that the active sites of goose deoxycholic and linolenic acid molecules and their protonated molecules are mainly distributed on -COOH, -OH and C=C. The results of MD simulation show that these molecules can be stably adsorbed in parallel on the Fe(110) surface through the active sites, resulting in better corrosion inhibition.

Acknowledgments

Funding support from National Natural Science Foundation of China(32360362)，National Natural Science Foundation of China(52161016), Joint Key Project of Agricultural Fundamental Research in Yunnan Province(202301BD070001-158 ， 202101BD070001-017),Open Fund Project of National Joint Engineering Research Center for Highly-Efficient Utilization Technology of Forestry Resources, Southwest Forestry University (2023-GC09) and Yunnan University Student Innovation and Entrepreneurship Training Program(20221054023).

Conflict of Interest

There is no conflict of interest.

Supporting Information

Not applicable.

CRediT Statement

Liqing Tang: Writing-original draft, Methodology, Data curation. **Min Tang:** Writing-review & editing, Methodology. **Ping Zhu:** Writing- review & editing, Supervision, Software, Conceptualization. **Xianghong Li:** Writing- review & editing, Supervision, Conceptualization. **Yun Gao:** Writing -review & editing, Methodology, Data curatio. **Yi Zhang:** Methodology, Data curation. **Yingju Miao:** Writing- review & editing, Supervision, Conceptualization. **JuanXu:** Writing-review & editing, Supervision, Conceptualization.

References

[1] Y. Zhao, T. Pan, X. Yu, D. Chen, Corrosion inhibition efficiency of triethanolammonium dodecylbenzene sulfonate on Q235 carbon steel in simulated concrete pore solution, *Corrosion Science*, 2019, **158**, 108097, doi: 10.1016/j.corsci.2019.108097.

[2] H. Hatayama, I. Daigo, Y. Matsuno, Y. Adachi, Outlook of the world steel cycle based on the stock and flow dynamics, *Environmental Science & Technology*, 2010, **44**, 6457-6463, doi: 10.1021/es100044n.
[3] Y. Xu, L. Yu, Y. Chen, Y. Tian, C. Liu, J. Wang, G. Liu, Y. Bai, C. Guo, J. Liu, P. Zhang, Evaluation of the anticorrosion properties of passivation solution containing different metal ions coated on a steel surface, *Engineered Science*, 2023, **24**, doi: 10.30919/es917.
[4] A. Carrozza, M. Cabrini, S. Lorenzi, M. Lombardi, T. Pastore, Improving the corrosion performance of LPBF- and EBM-processed Ti-6Al-4V by chemical pickling, *Engineered Science*, 2023, **26**, doi: 10.30919/es985.
[5] Sheetal, A. Kumar Singh, S. Thakur, B. Pani, M. Singh, Heterocyclic compounds as corrosion inhibitors for iron alloys in various industrial processes: A review, *Journal of Industrial and Engineering Chemistry*, 2024, **130**, 141-177, doi: 10.1016/j.jiec.2023.10.005.
[6] K. Xhanari, M. Finšgar, Organic corrosion inhibitors for aluminium and its alloys in acid solutions: a review, *RSC Advances*, 2016, **6**, 62833-62857, doi: 10.1039/C6RA11818F.
[7] Y. El aoufir, S. Zehra, H. Lgaz, A. Chaouiki, H. Serrar, S. Kaya, R. Salghi, S. K. AbdelRaheem, S. Boukhris, A. Guenbour, I.-M. Chung, Evaluation of inhibitive and adsorption behavior of thiazole-4-carboxylates on mild steel corrosion in HCl, *Colloids and Surfaces A*: *Physicochemical and Engineering Aspects*, 2020, **606**, 125351, doi: 10.1016/j.colsurfa.2020.125351.
[8] A. Dehghani, G. Bahlakeh, B. Ramezanzadeh, M. Ramezanzadeh, Potential role of a novel green eco-friendly inhibitor in corrosion inhibition of mild steel in HCl solution: Detailed macro/micro-scale experimental and computational explorations, *Construction and Building Materials*, 2020, **245**, 118464, doi: 10.1016/j.conbuildmat.2020.118464.
[9] P. I. Murungi, A. A. Sulaimon, Ideal corrosion inhibitors: a review of plant extracts as corrosion inhibitors for metal surfaces, *Corrosion Reviews*, 2022, **40**, 127-136, doi: 10.1515/corrrev-2021-0051.
[10], R. Jalham, G. Roymahapatra, M. K. Dash, O. Dagdag, L. Guo, In Silico studies on Triazole derivatives as corrosion inhibitors on mild steel in acidic media, *ES Materials & Manufacturing*, 2023, **21**, doi: 10.30919/esmm5f867.
[11] P. Du, S. Deng, G. Du, D. Shao, D. Xu, X. Li, Synergistic inhibition effect of Mikania micrantha extract with potassium iodide on the corrosion of cold rolled steel in methanesulfonic acid solution, *Corrosion Science*, 2023, **220**, 111296, doi: 10.1016/j.corsci.2023.111296.
[12] G. Wei, S. Deng, X. Li, Eupatorium Adenophora (Spreng.) leaves Extract as a Highly Efficient Eco-friendly Inhibitor for Steel Corrosion in trichloroacetic acid Solution, *International Journal of Electrochemical Science*, 2022, **17**, 221182, doi: 10.20964/2022.11.63.
[13] M. M. Alemnezhad, A. Ghaffarinejad, F. Omidali, White turnip bark extract as a new green and cost-effective corrosion bio-inhibitor for carbon steel in 1.0 M HCl solution: experimental and theoretical studies, *Chemical Physics Letters*, 2023, **831**, 140855, doi: 10.1016/j.cplett.2023.140855.
[14] X. Liu, Y. Gao, J. Guan, Q. Zhang, Y. Lin, C. Shi, Y. Wang, J. Du, N. Ma, Corrosion inhibition properties of spinach extract on Q235 steel in a hydrochloric acid medium, *Arabian Journal of Chemistry*, 2023, **16**, 105066, doi: 10.1016/j.arabjc.2023.105066.
[15] Y. Wang, Y. Qiang, H. Zhi, B. Ran, D. Zhang, Evaluating the synergistic effect of maple leaves extract and iodide ions on corrosion inhibition of Q235 steel in H_2SO_4 solution, *Journal of Industrial and Engineering Chemistry*, 2023, **117**, 422-433, doi: 10.1016/j.jiec.2022.10.030.
[16] H. Cang, Z. Fei, H. Xiao, J. Huang, Q. Xu, Inhibition effect of reed leaves extract on steel in hydrochloric acid and sulphuric acid solutions, *International Journal of Electrochemical Science*, 2012, **7**, 8869-8882, doi: 10.1016/S1452-3981(23)18038-2.
[17] X. Ma, J. Wang, J. Xu, J. Jing, J. Li, H. Zhu, S. Yu, Z. Hu, Sunflower head pectin with different molecular weights as promising green corrosion inhibitors of carbon steel in hydrochloric acid solution, *ACS Omega*, 2019, **4**, 21148-21160, doi: 10.1021/acsomega.9b02570.
[18] M. Zdravković, V. Grekulović, J. Suljagić, D. Stanković, S. Savić, M. Radovanović, U. Stamenković, Influence of blackberry leaf extract on the copper corrosion behaviour in 0.5 M NaCl, *Bioelectrochemistry*, 2023, **151**, 108401, doi: 10.1016/j.bioelechem.2023.108401.
[19] F. Kaya, R. Solmaz, İ. H. Geçibesler, Investigation of adsorption, corrosion inhibition, synergistic inhibition effect and stability studies of Rheum ribes leaf extract on mild steel in 1 M HCl solution, *Journal of the Taiwan Institute of Chemical Engineers*, 2023, **143**, 104712, doi: 10.1016/j.jtice.2023.104712.
[20] A. H. J. Mofidabadi, A. Dehghani, G. Bahlakeh, B. Ramezanzadeh, Combined clove extract bio-molecules and zinc(II) ion synergistic effects in steel corrosion mitigation in saline solution: electronic (DFT) modeling, atomic/molecular (MC/MD) simulations, and corrosion measurement, *Biomass Conversion and Biorefinery*, 2024, **14**, 9519-9539, doi: 10.1007/s13399-022-03002-1.
[21] X. Li, S. Deng, Inhibition effect of Dendrocalamus brandisii leaves extract on aluminum in HCl, H_3PO_4 solutions, *Corrosion Science*, 2012, **65**, 299-308, doi: 10.1016/j.corsci.2012.08.033.
[22] L. Guo, R. Zhang, B. Tan, W. Li, H. Liu, S. Wu, Locust Bean Gum as a green and novel corrosion inhibitor for Q235 steel in 0.5 M H_2SO_4 medium, *Journal of Molecular Liquids*, 2020, **310**, 113239, doi: 10.1016/j.molliq.2020.113239.
[23] S. H. Alrefaee, K. Y. Rhee, C. Verma, M. A. Quraishi, E. E. Ebenso, Challenges and advantages of using plant extract as inhibitors in modern corrosion inhibition systems: Recent advancements, *Journal of Molecular Liquids*, 2021, **321**, 114666, doi: 10.1016/j.molliq.2020.114666.
[24] G. Ji, S. K. Shukla, P. Dwivedi, S. Sundaram, R. Prakash, Inhibitive effect of*Argemone mexicana*Plant extract on acid corrosion of mild steel, *Industrial & Engineering Chemistry Research*, 2011, **50**, 11954-11959, doi: 10.1021/ie201450d.
[25] J. Liu, L. Qu, F. Wang, Z. Mei, X. Wu, B. Wang, H. Liu, L. He, A study on the anti-senescent effects of flavones derived from Prinsepia utilis Royle seed residue, *Journal of*

Ethnopharmacology, 2024, **328**, 118021, doi: 10.1016/j.jep.2024.118021.
[26] K. Chauhan, Y. C. Tripathi, V. K. Varshney, Prinsepia utilis Royle: A review on its traditional uses, phytochemistry, and biological activities, *Phytochemistry Letters*, 2023, **55**, 44-55, doi: 10.1016/j.phytol.2023.03.009.
[27] Y. Tu, R. An, H. Gu, N. Li, H. Yan, H.-Y. Liu, L. He, The water extracts from the oil cakes of Prinsepia utilis repair the epidermal barrier *via* up-regulating Corneocyte Envelope-proteins, lipid synthases, and tight junction proteins, *Journal of Ethnopharmacology*, 2024, **330**, 118194, doi: 10.1016/j.jep.2024.118194.
[28] P. Kewlani, D. C. Tewari, L. Singh, V. S. Negi, I. D. Bhatt, V. Pande, Saturated and polyunsaturated fatty acids rich populations of prinsepia utilis royle in western Himalaya, *Journal of Oleo Science*, 2022, **71**, 481-491, doi: 10.5650/jos.ess21262.
[29] H. Wu, S. Deng, D. Shao, G. Wei, J. Xu, X. Li, Synergistic mixture of Parthenium hysterophorus L. extract and potassium iodide as a novel efficient composite inhibitor on steel corrosion in sulfuric acid, *Journal of Materials Research and Technology*, 2025, **34**, 1704-1720, doi: 10.1016/j.jmrt.2024.12.178.
[30] H. Li, G. Wei, S. Deng, B. Tan, X. Li, Octadecyl dimethyl benzyl ammonium chloride as a novel efficient inhibitor for cold rolled steel in sulfuric acid, *Colloids and Surfaces A: Physicochemical and Engineering Aspects*, 2025, **715**, 136680, doi: 10.1016/j.colsurfa.2025.136680.
[31] A. T. Jeeja Rani, A. Thomas, M. Arshad, A. Joseph, The influence of aqueous and alcoholic extracts of Garcinia cambogia fruit rind in the management of mild steel corrosion in hydrochloric acid: Theoretical and electroanalytical studies, *Journal of Molecular Liquids*, 2022, **346**, 117873, doi: 10.1016/j.molliq.2021.117873.
[32] J. Chen, Y. Wu, L. Guo, W. Li, B. Tan, A. Brahmia, Insight into the anti-corrosion mechanism of Pisum sativum L leaves extract as the degradable inhibitor for Q235 steel in sulfuric acid medium, *Journal of the Taiwan Institute of Chemical Engineers*, 2023, **143**, 104664, doi: 10.1016/j.jtice.2022.104664.
[33] I. Langmuir, The constitution and fundamental properties of solids and liquids. part i. solids, *Journal of the American Chemical Society*, 1916, **38**, 2221-2295, doi: 10.1021/ja02268a002.
[34] M. HosseinpourRokni, R. Naderi, M. Soleimani, E. Kowsari, M. Pourfath, Indirect interactions between the ionic liquid and Cu surface in 0.5 M HCl: a novel mechanism explaining cathodic corrosion inhibition, *Corrosion Science*, 2023, **216**, 111100, doi: 10.1016/j.corsci.2023.111100.
[35] Q. Shi, S. Deng, B. Fan, D. Xu, J. Xu, X. Li, Rapeseed cake meal extract as an eco-friendly green sustainable inhibitor for the corrosion of cold rolled steel in trichloroacetic acid solution, *Journal of Materials Science & Technology*, 2025, **218**, 71-87, doi: 10.1016/j.jmst.2024.08.035.
[36] G. Wei, S. Deng, D. Shao, D. Xu, . Lei, X. Li, Gemini cationic surfactant of 1, 3-bis (dodecyl dimethyl ammonium chloride) propane as a novel excellent inhibitor for the corrosion of cold rolled steel in HCl solution, *Journal of Colloid and Interface Science*, 2025, **677**, 324-345, doi: 10.1016/j.jcis.2024.07.229.
[37] M. Tang, S. Deng, J. Xu, D. Xu, D. Shao, Q. Qu, X. Li, Invasive weed of Mikania micrantha extract as a novel efficient inhibitor for the corrosion of aluminum in HNO_3 solution, *Colloids and Surfaces A: Physicochemical and Engineering Aspects*, 2024, **680**, 132687, doi: 10.1016/j.colsurfa.2023.132687.
[38] L. Tang, G. Mu, G. Liu, The effect of neutral red on the corrosion inhibition of cold rolled steel in 1.0 M hydrochloric acid, *Corrosion Science*, 2003, **45**, 2251-2262, doi: 10.1016/S0010-938X(03)00046-5.
[39] K. Zakaria, A. Hamdy, M. A. Abbas, O. M. Abo-Elenien, New organic compounds based on siloxane moiety as corrosion inhibitors for carbon steel in HCl solution: Weight loss, electrochemical and surface studies, *Journal of the Taiwan Institute of Chemical Engineers*, 2016, **65**, 530-543, doi: 10.1016/j.jtice.2016.05.036.
[40] C. Jiang, G.-F. Wei, X. Ding, G. Du, X. Li, D. Shao, Investigation of biodegradable surfactant as a corrosion inhibitor to the cold rolled steel in the membrane separation device process, *Journal of Colloid and Interface Science*, 2025, **678**, 795-807, doi: 10.1016/j.jcis.2024.09.029.
[41] B. P. Markhali, R. Naderi, M. Mahdavian, M. Sayebani, S. Y. Arman, Electrochemical impedance spectroscopy and electrochemical noise measurements as tools to evaluate corrosion inhibition of azole compounds on stainless steel in acidic media, *Corrosion Science*, 2013, **75**, 269-279, doi: 10.1016/j.corsci.2013.06.010.
[42] F. Zhang, S. Deng, G. Wei, X. Li, Alternanthera philoxeroides extract as a corrosion inhibitor for steel in Cl3CCOOH solution, *International Journal of Electrochemical Science*, 2023, **18**, 100057, doi: 10.1016/j.ijoes.2023.100057.
[43] H. Kumar, V. Yadav, Anu, S. K. Saha, N. Kang, Adsorption and inhibition mechanism of efficient and environment friendly corrosion inhibitor for mild steel: Experimental and theoretical study, *Journal of Molecular Liquids*, 2021, **338**, 116634, doi: 10.1016/j.molliq.2021.116634.
[44] B. Tan, S. Zhang, H. Liu, Y. Guo, Y. Qiang, W. Li, L. Guo, C. Xu, S. Chen, Corrosion inhibition of X65 steel in sulfuric acid by two food flavorants 2-isobutylthiazole and 1-(1, 3-Thiazol-2-yl) ethanone as the green environmental corrosion inhibitors: Combination of experimental and theoretical researches, *Journal of Colloid and Interface Science*, 2019, **538**, 519-529, doi: 10.1016/j.jcis.2018.12.020.
[45] C. Cao, On electrochemical techniques for interface inhibitor research, *Corrosion Science*, 1996, **38**, 2073-2082, doi: 10.1016/S0010-938X(96)00034-0.
[46] P. Arellanes-Lozada, V. Díaz-Jiménez, H. Hernández-Cocoletzi, N. Nava, O. Olivares-Xometl, N. V. Likhanova, Corrosion inhibition properties of iodide ionic liquids for API 5L X52 steel in acid medium, *Corrosion Science*, 2020, **175**, 108888, doi: 10.1016/j.corsci.2020.108888.
[47] M. Khayatkashani, N. Soltani, N. Tavakkoli, A. Nejatian, J. Ebrahimian, M. A. Mahdi, M. Salavati-Niasari, Insight into the corrosion inhibition of Biebersteinia multifida root extract for

carbon steel in acidic medium, *Science of the Total Environment*, 2022, **836**, 155527, doi: 10.1016/j.scitotenv.2022.155527.
[48] D.-H. Xia, C.-M. Deng, D. MacDonald, S. Jamali, D. Mills, J.-L. Luo, M. G. Strebl, M. Amiri, W. Jin, S. Song, W. Hu, Electrochemical measurements used for assessment of corrosion and protection of metallic materials in the field: A critical review, *Journal of Materials Science & Technology*, 2022, **112**, 151-183, doi: 10.1016/j.jmst.2021.11.004.
[49] Y. Zhang, N. Li, N. Ling, J. Zhang, L. Wang, Enhanced long-term corrosion resistance of Mg alloys by superhydrophobic and self-healing composite coating, *Chemical Engineering Journal*, 2022, **449**, 137778, doi: 10.1016/j.cej.2022.137778.
[50] Q. H. Zhang, B. S. Hou, Y. Y. Li, G. Y. Zhu, H. F. Liu, G. A. Zhang, Two novel chitosan derivatives as high efficient eco-friendly inhibitors for the corrosion of mild steel in acidic solution, *Corrosion Science*, 2020, **164**, 108346, doi: 10.1016/j.corsci.2019.108346.
[51] M. Lagrenée, B. Mernari, M. Bouanis, M. Traisnel, F. Bentiss, Study of the mechanism and inhibiting efficiency of 3, 5-bis(4-methylthiophenyl)-4H-1, 2, 4-triazole on mild steel corrosion in acidic media, *Corrosion Science*, 2002, **44**, 573-588, doi: 10.1016/S0010-938X(01)00075-0.
[52] T. Zheng, J. Liu, M. Wang, Q. Liu, J. Wang, Y. Chong, G. Jia, Synergistic corrosion inhibition effects of quaternary ammonium salt cationic surfactants and thiourea on Q235 steel in sulfuric acid: Experimental and theoretical research, *Corrosion Science*, 2022, **199**, 110199, doi: 10.1016/j.corsci.2022.110199.
[53] B. X. Vuong, T. L. Huynh, T. Q. N. Tran, S. V. Prabhakar Vattikuti, T. D. Manh, P. Nguyen-Tri, A. T. Nguyen, P. Van Hien, N. N. Dang, Corrosion inhibition of carbon steel in hydrochloric acid solution by self-formation of a Malpighia glabra leaf extract-based organic film, *Materials Today Communications*, 2022, **31**, 103641, doi: 10.1016/j.mtcomm.2022.103641.
[54] A. Kumar, C. Das, Corrosion inhibition of mild steel by Praecitrullus fistulosus (tinda fruit and peel) extracts, *Science of the Total Environment*, 2024, **929**, 172569, doi: 10.1016/j.scitotenv.2024.172569.
[55] S. Deng, X. Li, G. Du, An efficient corrosion inhibitor of cassava starch graft copolymer for aluminum in phosphoric acid, *Chinese Journal of Chemical Engineering*, 2021, **37**, 222-231, doi: 10.1016/j.cjche.2020.08.013.
[56] H. Li, Y. Qiang, W. Zhao, S. Zhang, 2-Mercaptobenzimidazole-inbuilt metal-organic-frameworks modified graphene oxide towards intelligent and excellent anti-corrosion coating, *Corrosion Science*, 2021, **191**, 109715, doi: 10.1016/j.corsci.2021.109715.
[57] X. Teng, S. Deng, X. Li, Synergistic corrosion inhibition of rubber seed extract with KI on cold rolled steel in sulfuric acid solution, *Journal of the Taiwan Institute of Chemical Engineers*, 2024, **161**, 105564, doi: 10.1016/j.jtice.2024.105564.
[58] X. Li, S. Deng, G. Du, Nonionic surfactant of coconut diethanolamide as a novel corrosion inhibitor for cold rolled steel in both HCl and H_2SO_4 solutions, *Journal of the Taiwan Institute of Chemical Engineers*, 2022, **131**, 104171, doi: 10.1016/j.jtice.2021.104171.
[59] H. Idriss, On the wrong assignment of the XPS O1s signal at 531–532 eV attributed to oxygen vacancies in photo- and electro-catalysts for water splitting and other materials applications, *Surface Science*, 2021, **712**, 121894, doi: 10.1016/j.susc.2021.121894.
[60] L. Monaco, R. N. S. Sodhi, G. Palumbo, U. Erb, XPS study on the passivity of coarse-grained polycrystalline and electrodeposited nanocrystalline nickel-iron (NiFe) alloys, *Corrosion Science*, 2020, **176**, 108902, doi: 10.1016/j.corsci.2020.108902.
[61] O. Olivares-Xometl, N. V. Likhanova, M. A. Domínguez-Aguilar, J. M. Hallen, L. S. Zamudio, E. Arce, Surface analysis of inhibitor films formed by imidazolines and amides on mild steel in an acidic environment, *Applied Surface Science*, 2006, **252**, 2139-2152, doi: 10.1016/j.apsusc.2005.03.178.
[62] X. Zhao, J. Hu, J. Nie, D. Chen, G. Qin, E. Zhang, Enhanced antibacterial activity, corrosion resistance and endothelialization potential of Ti-5Cu alloy by oxygen and nitrogen plasma-based surface modification, *Journal of Materials Science & Technology*, 2024, **168**, 250-264, doi: 10.1016/j.jmst.2023.04.076.
[63] X. Wang, Q. Zhang, H. Jiang, Y. Gu, X. Li, L.-L. Xu, Pueraria Lobata leaf extract as green corrosion inhibitor for low carbon steel in 1.0M HCl solution, *Research on Chemical Intermediates*, 2021, **47**, 1051-1069, doi: 10.1007/s11164-020-04316-3.
[64] X. Sun, L. He, P. Zhang, X. Zhang, Effect of hydrocarbon chain length of alkyl trimethyl ammonium bromide on corrosion inhibition of stainless steel in sulfuric acid, *Journal of Solid State Electrochemistry*, 2024, **28**, 3697-3711, doi: 10.1007/s10008-024-05966-8.
[65] N. Wazzan, I. B. Obot, T. M. Fagieh, The role of some triazoles on the corrosion inhibition of C1020 steel and copper in a desalination descaling solution, *Desalination*, 2022, **527**, 115551, doi: 10.1016/j.desal.2022.115551.
[66] A. Salmasifar, M. Edraki, E. Alibakhshi, B. Ramezanzadeh, G. Bahlakeh, Theoretical design coupled with experimental study of the effectiveness of the inhibitive molecules based on Cynara scolymus L extract toward chloride-induced corrosion of steel, *Journal of Molecular Liquids*, 2021, **332**, 115742, doi: 10.1016/j.molliq.2021.115742.
[67] S. K. Saha, P. Ghosh, A. Hens, N. C. Murmu, P. Banerjee, Density functional theory and molecular dynamics simulation study on corrosion inhibition performance of mild steel by mercapto-quinoline Schiff base corrosion inhibitor, *Physica E: Low-Dimensional Systems and Nanostructures*, 2015, **66**, 332-341, doi: 10.1016/j.physe.2014.10.035.
[68] K. Fukui, Role of frontier orbitals in chemical reactions, *Science*, 1982, **218**, 747-754, doi: 10.1126/science.218.4574.747.
[69] G. Laadam, M. El Faydy, F. Benhiba, T. A., H. Amegroud, A. S. Al-Gorair, H. Hawsawi, R. Touzani, I. Warad, A. Bellaouchou, A. Guenbour, M. Abdallah, A. Zarrouk, Outstanding anti-corrosion performance of two pyrazole derivatives on carbon steel in acidic medium: Experimental and quantum-chemical examinations, *Journal of Molecular Liquids*, 2023, **375**, 121268, doi: 10.1016/j.molliq.2023.121268.

[70] N. Kovačević, A. Kokalj, The relation between adsorption bonding and corrosion inhibition of azole molecules on copper, *Corrosion Science*, 2013, **73**, 7-17, doi: 10.1016/j.corsci.2013.03.016.
[71] A. Thoume, D. Benmessaoud Left, A. Elmakssoudi, F. Benhiba, A. Zarrouk, N. Benzbiria, I. Warad, M. Dakir, M. Azzi, M. Zertoubi, Chalcone oxime derivatives as new inhibitors corrosion of carbon steel in 1 M HCl solution, *Journal of Molecular Liquids*, 2021, **337**, 116398, doi: 10.1016/j.molliq.2021.116398.
[72] M. Shahraki, M. Dehdab, S. Elmi, Theoretical studies on the corrosion inhibition performance of three amine derivatives on carbon steel: Molecular dynamics simulation and density functional theory approaches, *Journal of the Taiwan Institute of Chemical Engineers*, 2016, **62**, 313-321, doi: 10.1016/j.jtice.2016.02.010.
[73] R. R. Annand, R. M. Hurd, N. Hackerman, Adsorption of monomeric and polymeric amino corrosion inhibitors on steel, *Journal of the Electrochemical Society*, 1965, **112**, 138, doi: 10.1149/1.2423482.
[74] M. A. Quraishi, A. Singh, V. K. Singh, D. K. Yadav, A. K. Singh, Green approach to corrosion inhibition of mild steel in hydrochloric acid and sulphuric acid solutions by the extract of Murraya koenigii leaves, *Materials Chemistry and Physics*, 2010, **122**, 114-122, doi: 10.1016/j.matchemphys.2010.02.066.
[75] A. Phukaoluan, K. Srirussamee, A. Khantachawana, M. Chuchonak, P. Tunthawiroon, Influence of the oxide film on the performance and corrosion resistance of TiNiCu shape memory alloys as the heat engine actuator, *Engineered Science*, 2024, **31**, doi: 10.30919/es1226.